Micro graphite-patterned diamond sensors: Towards the simultaneous in vitro detection of molecular release and action potentials generation from excitable cells

Micrographite-patterned diamond sensors: towards the simultaneous *in vitro* detection of molecular release and action potentials generation from excitable cells

Giulia Tomagra[1,†], Pietro Aprà[2,3,†], Alfio Battiato[3], Cecilia Collà Ruvolo[2], Alberto Pasquarelli[4], Andrea Marcantoni[1], Emilio Carbone[1], Valentina Carabelli[1], Paolo Olivero[2,3], Federico Picollo[2,3,*]

[1] Department of Drug and Science Technology and "NIS" inter-departmental centre, University of Torino, Corso Raffaello 30, 10125 Torino, Italy

[2] Department of Physics and "NIS" inter-departmental centre, University of Torino, Via Pietro Giuria 1, 10125 Torino, Italy

[3] Istituto Nazionale di Fisica Nucleare, sezione di Torino, Via Pietro Giuria 1, 10125 Torino, Italy

[4] Institute of Electron Devices and Circuits, University of Ulm, 89069 Ulm, Germany

* corresponding author. E-mail: federico.picollo@unito.it (Federico Picollo)

† these authors contributed equally to this work

In neuroscience, a deep understanding of communication mechanisms at the cellular level is of paramount importance, since their dysfunction determines the onset of several diseases. The development of innovative sensors devoted to the investigation of both chemical and electrical signals it is therefore essential to improve the outcome of standard trials and to define novel methodologies.

Here we report on the fabrication and the characterization of multi-functional micrographite patterned diamond multi-electrode arrays. These sensors are obtained by means of a three-dimensional patterning process of single-crystal diamond substrates by means of MeV ion-beam-based lithography, which allows the direct fabrication of graphitic micro-channels embedded within the bulk of the electrically insulating diamond matrix.

Proof-of-concept *in vitro* experiments on cultured neurons and cardiac tissue were performed, in which quantal secretory events were amperometrically recorded from dopaminergic neurons, while potentiometric measurements of action potential generation were collected from both hippocampal neuronal networks and intact sinoatrial nodes.

These achievements represent the demonstration of the applicability of an all-carbon hybrid graphite/diamond device for the multi parametric detection of chemical and electrical signals, thus

representing a fundamental step for the simultaneous *in vitro* measurement of the two types of signals from the same biological sample.

1. Introduction

The main mechanisms regulating the intra- and extra-cellular communication in neurons and neuroendocrine cells are based on two distinct phenomena: the neurotransmitter release and the action potential generation. The former consists of the quantal release of bioactive molecules from secretory vesicles into the extracellular environment. This process is based on the fusion of presynaptic vesicles with the plasma membrane and, in the context of neurotransmission, the release occurs into the synaptic cleft by means of a calcium-triggered mechanism [1–3]. The latter depends by somatic action potential (AP) generation and its propagation through axon fibers to the presynaptic terminal where the variation of the membrane potential induces the opening of voltage-gated calcium channels and the onset of Ca^{2+}-dependent synaptic transmission. The AP generation and propagation is specific of all excitable cells and modulate other physiological function such as hormonal release and muscle contraction [4–6]. Dysfunctions involving these mechanisms determine the onset of several neuropsychiatric and neurological disorders such as Alzheimer, Parkinson and Huntington diseases.

The development of sensors devoted to the detection of both these types of signals becomes of paramount importance, because it would allow performing *in vitro* experiments in which molecular and structural mechanism or drugs efficacy could be investigated at the cellular level. To this scope, different devices are now widely adopted to record either the secretory or electrical activities. Carbon fibre microelectrodes (CFE) are employed since decades for the acquisition of exocytotic events by amperometric measurements [7], providing information on key mechanisms such as the fusion pore formation and the kinetics of the single vesicle secretion in real time. Complementarily, potentiometric multi-electrodes arrays (MEA) are realized to detect patterns of action potentials through different types of substrates using large numbers of microelectrodes (i.e. up to thousands). In this context, few prototypal demonstrators have been so far developed to perform both types of measurements from the same biological samples [8], but a robust and easy-to-use device to this scope is not yet available.

Diamond-based MEA represent a promising solution to this technological demand. In fact, the peculiar properties of diamond make it an ideal substrate for biosensing due to the optimal biocompatibility [9–11]

that is essential for long-term culture, chemical inertness that avoids interaction with culture medium, wide optical transparency window that makes it usable with fluorescence microscopy, and lower absorption of organic molecules that minimizes electrode fouling [12]. The electrical properties of diamond substrates can be modified by means of either doping [13,14] or inducing a transition to the graphitic phase [15–18], thus allowing the realization of conductive electrodes.

Up to date, only a limited number of works on diamond-based sensors of exocytic activity have shown that boron-doped structures can be employed as recording electrodes for the real-time investigation of neurotransmitters release [19–22].

On the other hand, several works explored the possibility of exploiting boron-doped diamond for the recording of electrical biosignals from different cellular systems. Multi-electrode planar arrays were employed both to monitor the cardiac action potentials [23] and to interface with neuronal networks [24,25], while flexible sensors were developed with the aim of fabricating retinal prostheses [26,27]. Significant improvements in the performances of diamond devices were also explored by means of 3D-structuring of the electrodes, in order to create high-aspect-ratio microstructures optimized for neuronal action potential detection [28,29]. Fabrication approaches alternative to the boron doping were based on surface hydrogen termination [30] or solution-gate field-effect transistors [31] and were adopted for the development of sensors dedicated to action potential recording from excitable cells.

In this work we demonstrate that cellular sensors based on embedded graphitic micro-channels in diamond substrates can be successfully applied for the investigation of both types of cellular signal mechanisms. The applicability of these biosensors for the real-time amperometric detection of quantal exocytotic events from chromaffin cells was already reported in previous papers [32–34]. In this work, we report on their capability of measuring secretory signals also from neurons, and moreover we demonstrate the possibility of recording action potentials from cardiac tissues and neuronal networks.

2. Experimental

2.1 Device fabrication

The sensors were fabricated in high-purity artificial polycrystalline diamond substrates produced by chemical vapour deposition by Diamond Material (Freiburg, Germany). The substrates are 5×5×0.4 μm^3 in

size and are classified as type IIa optical grade, guaranteeing both nitrogen and silicon defect concentration of less than 10 ppm. The larger surfaces have a roughness of < 5 nm as reported by the producer.

The fabrication of embedded graphitic microchannels can be obtained by means of MeV Ion Beam Lithography, a fabrication technique based on the introduction of structural defects in the crystal lattice due to the nuclear interaction between carbon atoms and implanted ions. This approach allows the controlled variation of the optical [35–37], mechanical [38–41] and electrical properties [15–17,42,43] of the target material. More specifically, the creation of electrically conductive electrodes for cellular sensing is achieved by promoting the phase transition of diamond into graphite, which can be obtained upon high-temperature thermal treatment in regions of the crystal where the ion-beam-induced defect density overcomes a critical threshold, usually referred as graphitization threshold [40,44,45]. The main peculiarity of this fabrication scheme is represented by the possibility of fine-tuning the localization of these effects by the control of ion beam energy, thus guaranteeing the creation of structures with high spatial resolution in the three spatial dimensions (see Fig 1a and 1b).

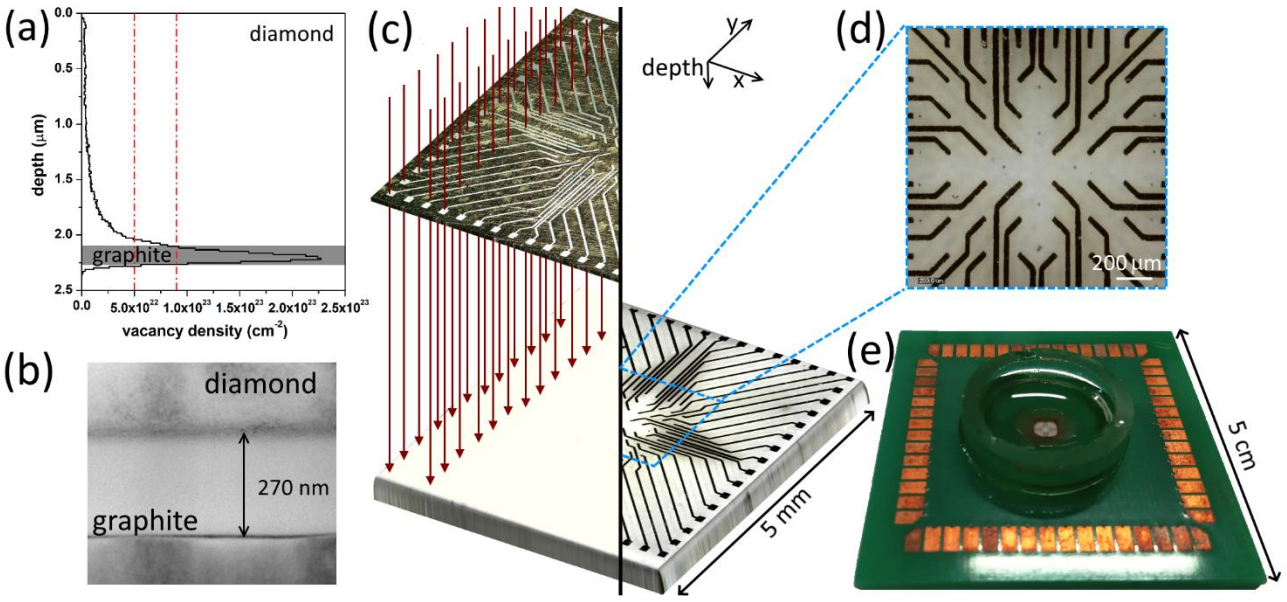

Figure 1 – (a) SRIM Monte Carlo [46] simulation of vacancy density induced in diamond by 1.8 MeV He^+ irradiation. Dashed lines indicate the range of graphitization threshold reported in literature. (b) A cross-section TEM image of a graphitic channel. (c) Schematic of the implantation process (left side) and obtained sensor (right side). (d) Optical image of the sensor central region. (e) Picture of assembled μG-D-MEA.

A collimated 1.3 MeV He^+ beam with a current density of 1.5 μA cm^{-2} was employed for the fabrication of the electrodes of the micro-graphite-patterned diamond multi electrode array (μG-D-MEA). This process was performed at the AN2000 accelerator of the Legnaro National Laboratories of the Italian Institute of Nuclear Physics (LNL-INFN) [47–49]. The fluence was set to 1×10^{17} cm^{-2} in order to overcome the graphitization threshold in correspondence of a ~270 nm thick region located at a depth of ~2.2 μm below the sample surface. Further details on the fabrication process are present in the supporting information.

The obtained devices present 60 independent graphitic electrodes whose emerging central end-points are arranged as an 8×8 matrix with ~200 μm spacing, while in the peripheral region of the diamond the corresponding emerging end-points are distributed 15 per side and are ~180 μm spaced (see figure 1c). Finally, the μG-D-MEA were mounted on chip carriers that were specifically developed to suitably interface with the commercially available signal acquisition chain produced by MultiChannels System (model MEA1060-Inv-BC). Furthermore, the chip carriers were equipped with a small container for the culture solutions, as shown in figure 1e, and an Ag/AgCl reference electrode which is directly immersed into the container.

2.2 Device characterization

Preliminary Raman and electrical measurements were performed to assess both the structural and electrical properties of the conductive micro-channels, thus confirming the effectiveness of the fabrication steps.

Raman spectra were acquired with a Horiba Jobin Yvon HR800 Raman micro-spectrometer equipped with a 600 lines mm^{-1} diffraction grating, a continuous 532 nm excitation laser focused with a 100× air objective and a CCD detection system. This setup guarantees the collection of spectra with a spatial resolution of ~2 μm both in diameter and in focal depth, and spectral resolution of ~3 cm^{-1}.

Figures 2a-d show four Raman spectra collected from different regions of the device, namely: a nominally unirradiated region of the diamond substrate far from the microchannels, a region of the diamond substrate close of few micrometers to the micro-channel, a region in correspondence of the very emerging end-point of the microchannel and a region of the diamond substrate located directly above the sub-superficial graphitic channel.

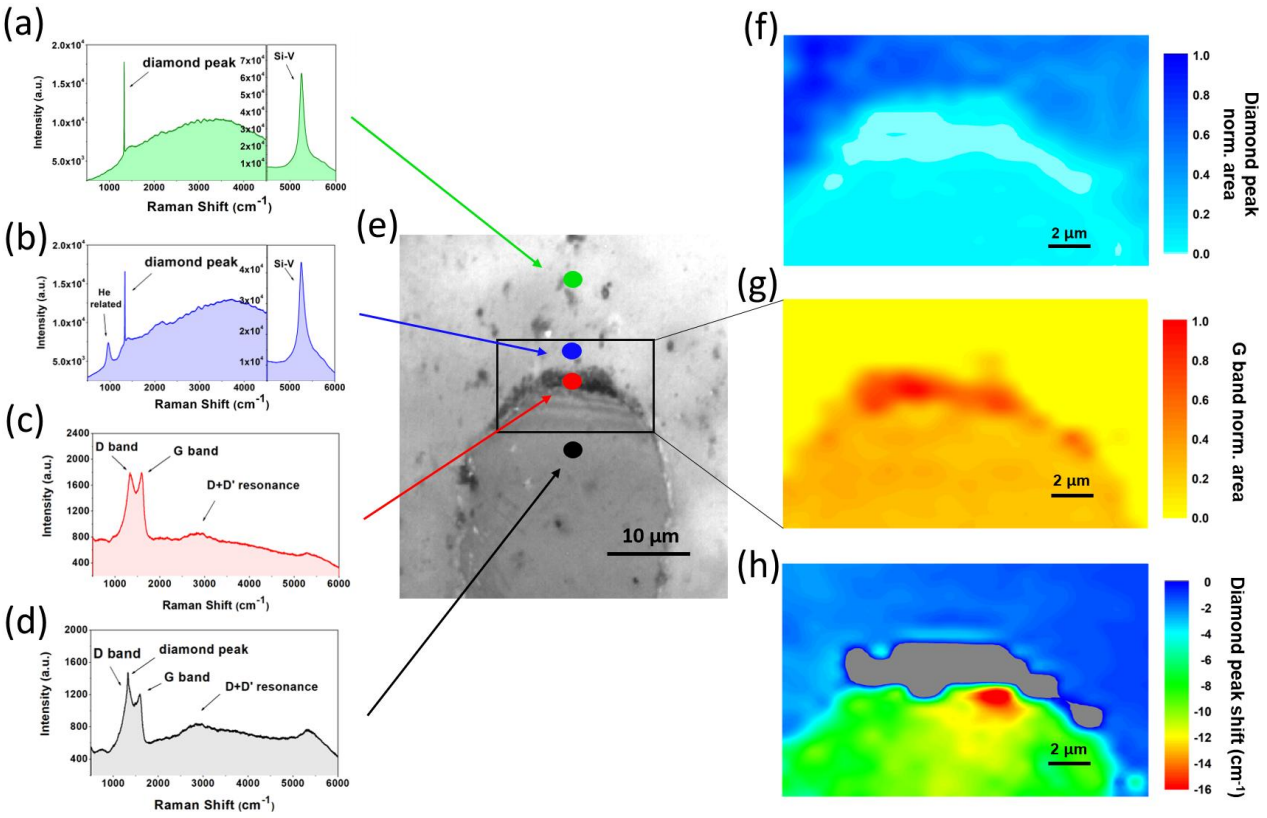

Figure 2 - Raman spectra collected from the diamond (a), the diamond near the channel (b), the exposed graphitic of the channel emerging region (c) and over channel (d). The location of these analysis points is indicated in the optical image (e). Diamond peak (f) and G band (g) intensity maps are presented adopting a colour scale representing the normalized area of the integrated spectral range. (h) Spatial map of diamond internal stress induced by ion beam lithography fabrication evaluated as a shift of diamond Raman peak. Grey regions indicate the absence of diamond peak contribution.

The spectra collected from the first and second regions (green and blue spots in figures 2e) exhibit the characteristic first-order Raman peak of diamond at 1332 cm^{-1} and the luminescence signals associated to the Silicon-Vacancy colour centres (SiV) located at 5260 cm^{-1} (739 nm) [50] due to the silicon impurities incorporated during the growth of the crystal with no visible features related to amorphous or graphite-like phases (see figure 2a), thus confirming that the unprocessed areas of the substrate are indeed consisting of a pristine diamond phase even in close proximity of the channels' endpoints. Probing the material closer to the implanted structures (fig 2b), in addition to the diamond and SiV luminescence peaks, a feature appears at lower Raman shift (963 cm^{-1}, 561 nm), addressable to the He–related colour centres [51,52] consequently to the ion damaging performed with He^{+} in correspondence of the channel.

Differently, the spectra collected from the very endpoints of the sub-superficial microchannel (red spot in figure 2e) exhibit two broad bands at 1361 cm^{-1} and 1582 cm^{-1}, which are respectively referred as the D and G bands (figure 2c). These features are commonly attributed to amorphous sp^2 carbon-based system (D band) and to the stretching of the C - C bonds of graphitic carbon (G band) [53,54], thus providing a direct evidence of the exposure of graphite-like phase at the sample surface in correspondence of the very endpoints of the implanted channels. Moreover, a weaker and broader peak at 2835 cm^{-1} is addressable to D+D' Raman resonance. When probing the regions located directly above the channels (black spot in figure 2e), Raman features arising from both the diamond "cap layer" and the sub-superficial microstructures can be clearly observed despite a large spectral overlap between the first-order Raman peak and the D band (figure 2d). This evidence is compatible with expectations, if it is considered that the microchannel is located at a depth of ~1 μm, while the focal depth of the apparatus is ~2 μm.

In figures 2f and 2g, the spatial distributions of the normalized intensities of the first-order Raman peak of diamond and G band are respectively mapped. As expected, the intensity of the first-order diamond peak is significantly decreased in correspondence of the graphitic channel, and completely disappears in correspondence of the emerging region, where complementarily the intensity of the G band is maximized. From the analysis of the two maps the extension of the graphitic region exposed to the surface was estimated, resulting in an active detection area of ~2×10 μm^2. It is worth remarking that, following previous works on the fabrication of these types of embedded graphitic structures [16,18,55], these results represent the first direct evidence from structural measurements of the effective exposure of the graphitic-like phase to the sample surface, and most importantly of the effective area of the exposed region.

Moreover, figure 2h shows the spatial distribution of the spectral red-shift of the first-order Raman peak of diamond. Interestingly, this map can provide a direct evidence of the mechanical stresses applied to the diamond lattice by the constrained expansion of the lower-density graphitic channels lying below the sample surface. As expected, the volume expansion associated with the formation of the graphitic layer causes a maximum spectral red-shift (i.e. ~16 cm^{-1}, see the red-encoded area of figure 2h) in correspondence of the region where the graphitic structure is emerging at the substrate surface. The dependence of the Raman peak shift $\Delta\omega$ from the hydrostatic stress σ_h in diamond is given by the following empirical relation [56]:

$$\Delta\omega = a \cdot \sigma_h + b \cdot \sigma_h^2 \qquad (1)$$

where a = 2.83 cm^{-1} GPa^{-1} and b = $–3.65×10^{-3}$ cm^{-1} GPa^{-2}. Although undoubtedly a tensorial approach would be more appropriate to suitably deconvolute the different stress components, as already explored in previous works investigating the stress effect of graphitic inclusions in diamond [57], the above-mentioned formula can effectively provide a useful first-order estimation of the amount of local mechanical stress undergone by the diamond crystal surrounding the emerging graphitic structure. The maximum stress estimated from Eq. (1) would be ~5.7 GPa. Such a value, although apparently insufficient to create cracks or other mechanical failures around the emerging channel (as evident from the optical micrograph in figure 2e), is nonetheless remarkably higher than what was previously estimated with the same approach from non-emerging graphitic structures [58].

Using an approach adopted in previous works [16,59], current-voltage characterization of the graphitic structures was performed to evaluate the electrical properties of the electrodes. Figure 3a shows two-terminal I–V characteristics obtained with a probe station connected to the Keithley 2636 electrometer.

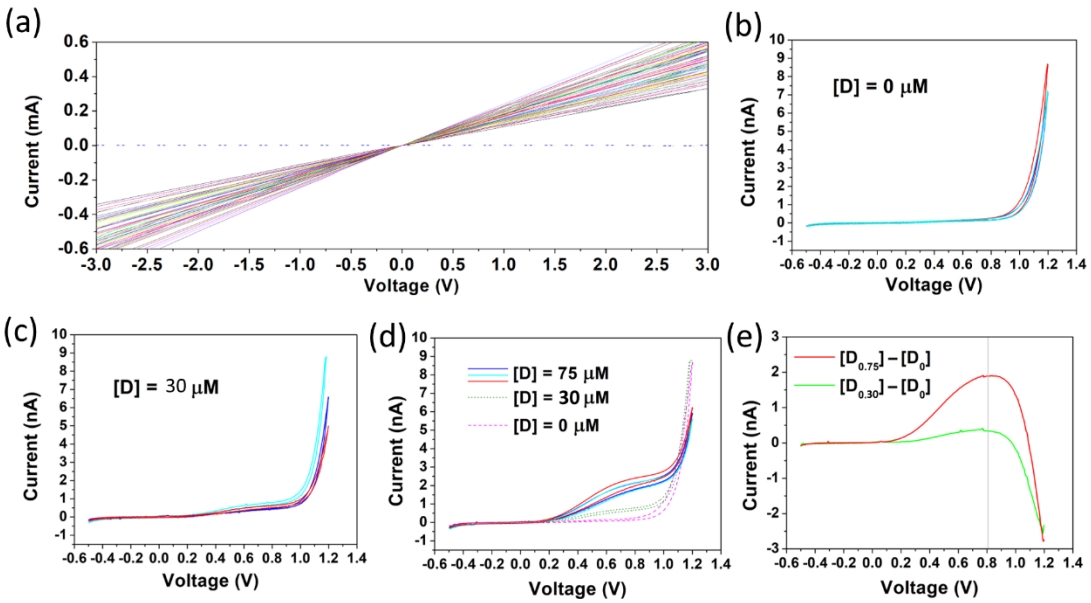

Figure 3 – (a) Current-voltage curves for the 60 channels of the biosensor. Cyclic voltammetry recorded from three representative channels from a saline solution containing dopamine at different concentration: 0 µM (b), 30 µM (c) and 75 µM (d). (e) Curve obtained by the subtraction of the rising branch of cyclic voltammetry recorded from solutions with [D] = 30 µM (green) and [D] = 75 µM (red) with those without dopamine.

The measurements were performed in the ±3 V voltage range at room temperature. Silver depositions were employed to reduce the contact resistance between the probe microtip and the graphitic electrodes and a pair of additional depositions were defined in a test region located far from the microstructures in order to rule out any parasitic conduction paths related to surface contaminations. The I-V characteristics acquired from these latter contacts is reported in figure 3a as dashed line and is indicative of a surface resistance that it is compatible with that of the electrometer (i.e. >1 TΩ). All the I-V characteristics collected from the microchannels exhibit an ohmic behaviour associated with resistance values ranging from 4 kΩ to 9 kΩ. This spread is can be entirely attributed to the different geometrical parameters of the channels. This is confirmed by the fact that the resistivity values estimated from the length and width of the channels (measured from the optical micrographs, figure 1c) as well as from their thickness (estimated from cross-sectional TEM measurements, figure 1b) are mutually consistent, and yield a mean value of (2.7 ± 0.3) mΩ cm. Such value is compatible with both previous reports [18,55] and with the expected resistivity of polycrystalline graphite, which is comprised between the resistivity values measured along the directions which are parallel (i.e. 0.5 mΩ cm) and perpendicular (i.e. 300 mΩ cm) to the graphitic planes [60].

2.3 Amperometric measurements

In previous works, the full functionality of the μG-D-MEA for the amperometric detection of quantal exocytotic events from neuroendocrine chromaffin cells was extensively demonstrated [32,34,61]. The employed devices consisted of multielectrode arrays equipped with 16 independent channels fabricated with the above-described lithographic technique, and interfaced with a custom-designed electronic chain. This configuration allowed the investigation of different neurotransmitters release mechanisms by means of the systematic recording of amperometric chronograms. In these measurements, upon setting the electrode bias to +800 mV and the sampling frequency to 4 kHz (low pass cut-off frequency = 1 kHz), relatively long events (half time width, $t_{1/2}$ = (16.0 ± 0.5) ms) of large amplitude (current amplitude, I_{max} = (73 ± 3) pA associated with the quantity of released adrenaline [62,63]) could be easily acquired.

Since the ultimate purpose of these sensors is to be the multi-parametric detection of both chemical and electrical signals from *in vitro* neuronal networks, in the following we report a proof-of-concept demonstration of the measurement of dopamine release from midbrain neurons. Since the process of the neurotransmitter release from neurons involves a significantly lower amount of secreted molecules that

generate oxidative currents in the order of few pA lasting fractions of ms, a substantial optimization of the acquisition parameter with respect to previous measurements was necessary [64,65]. In particular, by systematically analysing the signal-to-noise ratio of the bias applied to the electrodes by means of cyclic voltammetry we increased the sampling rate and low-pass band frequencies adopted with respect to previous measurements on chromaffin cells (see below).

Figures 3b-d report cyclic voltammetry plots of three representative channels performed with saline solutions (Tyrode) with different dopamine concentrations (namely, 0 μM, 30 μM and 75 μM). The measurements were performed by sweeping the electrode bias between -0.5 V and +1.2 V, with a scan rate of 20 mV s^{-1}. The reference recording acquired from the Tyrode solution with no dopamine (figure 3b) exhibits an electrochemical window comprised between -0.5 V and +0.8 V. Within such a window, the leakage current is <100 pA, thus allowing the detection of the oxidation of dopamine molecules that occurs in the +0.6 V ÷ +0.8 V range [66]. By analysing the difference between the curves collected from the solutions enriched with dopamine with respect to the reference one, it was possible to identify that the bias which optimizes the signal-to-noise ratio is ~800 mV, as shown in figure 3e.

Furthermore, systematic amperometric measurements from solutions characterized by increasing dopamine concentrations (i.e. 8 values in the 0÷100 μM range) were performed in order to evaluate the limit of detection (LOD) of the device which correspond to a concentration of 1 μM, which in turn corresponds to a limit of quantification LOQ = 3 × LOD ~3 μM. Figure 1SM from the Supplementary Material shows the dose-response curve obtained by averaging the data acquired over 25 s time intervals. This LOQ guarantees the detection of the neurotransmitter released from neuronal networks since the concentration of catecholamines stored into a single vesicle can reach hundreds of μM [67].

Concerning the sampling frequency, preliminary measurements of secretion from 12 days *in vitro* (DIV) midbrain neuron network were carried out by setting the sampling frequency at 8 kHz (pass-band 1 kHz) and 25 kHz (pass-band 4 kHz) with 800 mV electrode bias (figure 4).

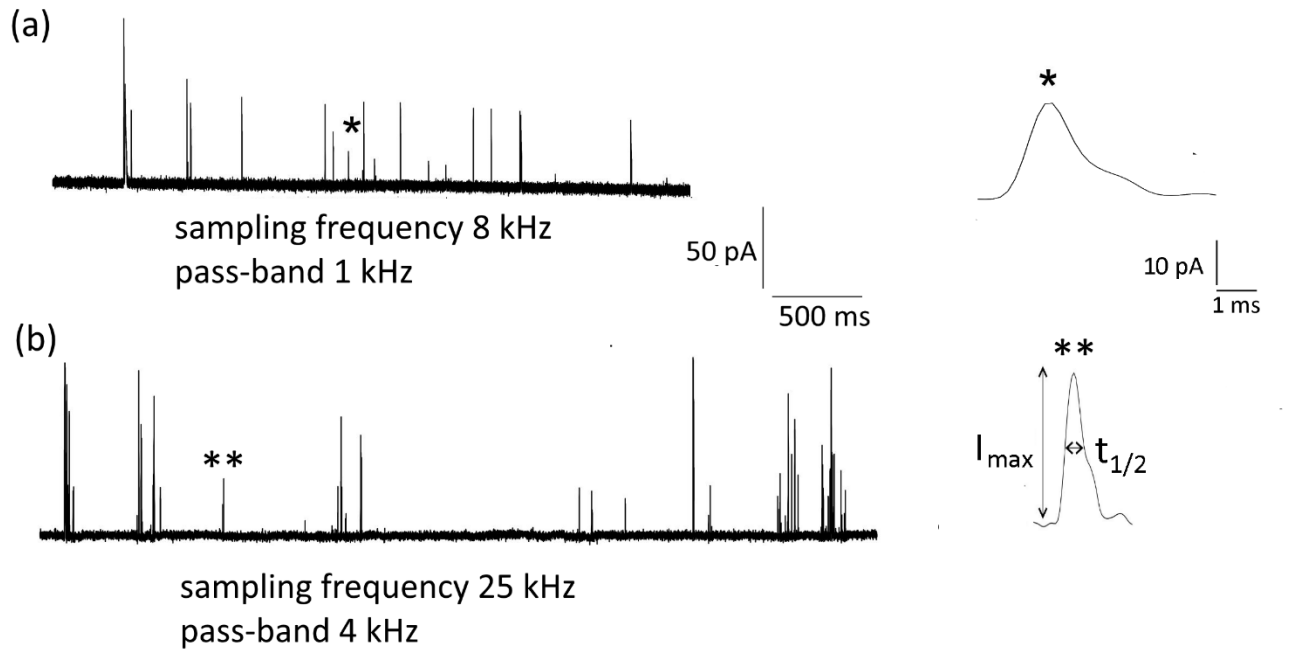

Figure 4 – Amperograms acquired at 8 kHz (a) and 25 kHz (b) reporting exocytotic events from dopaminergic neurons. Two exemplificative spikes collected with the different input parameters were magnified.

In order to enhance the intensity of the amperometric signals, the midbrain neurons were incubated with 20 µM levodopa, a precursor of dopamine which induces the increase of dopamine content in the vesicles [64]. From the analysis of the spikes acquired at 8 kHz sampling frequency, it can be noted that the mean values of the half-time width ($t_{1/2}$) and the maximum current (I_{max}) are equal to (2.8 ± 0.2) ms and (36 ± 4) pA, respectively; on the contrary, by setting the sampling frequency at 25 kHz, the signal parameters are $t_{1/2}$ = (0.65 ± 0.02) ms and I_{max} = (37 ± 3) pA. As it can be observed by comparing he two sampling rates, the former dataset presents a significant discrepancy in the $t_{1/2}$ values with respect to the data collected at higher sampling frequency Indeed, the inadequate low sampling rate and pass-band frequencies result in a significant overestimation of the half-time width, due to limitations in the discrimination of subsequent peaks. On the contrary, the higher sampling frequency guarantees a better time resolution of dopamine release events, thus representing the minimum acquisition frequency that should be adopted.

2.4 Potentiometric measurements

The action potential (AP) recordings were performed by employing a commercial "MCS MEA 1060-Inv-BC" amplifier from Multi Channel Systems (Reutlingen), since the µG-D-MEA was developed to be fully compatible with standard acquisition electronics. The sampling rate was set to 10 kHz. The acquisition by the µG-D-MEA was affected by a half-band noise of (35 ± 5) µV. Although slightly larger compared with the corresponding value of (22 ± 2) µV for a conventional Multi Electrode Array device, this noise level is lower enough to allow the detection of action potential both from tissue and neuronal networks, as reported in the following.

The first measurements were performed on the sinoatrial (SA) node, which is a tissue responsible for the pacemaker activity of miocardial tissue. This experimental model was chosen since it represents a simple benchmark sample generating large action potentials (i.e. ~300 µV) across the whole tissue surface.

The potentiometric measurement of the action potential generated by the SA node was performed both by means of conventional MEA sensors (60MEA200/300iR-Ti, Multi Channels System) and the µG-D-MEA, after placing the tissue in the centre of the recording area. Experiments were performed at room temperature.

Figures 5a and 5b show four representative traces of the spontaneous activity of the SA node, which fired at a mean basal frequency of (3.5 ± 0.4) Hz and (2.8 ± 0.6) Hz, respectively measured with µG-D-MEA and conventional MEA (frequencies values compatible at ANOVA test followed by Bonferroni *post hoc* comparison $p > 0.05$).

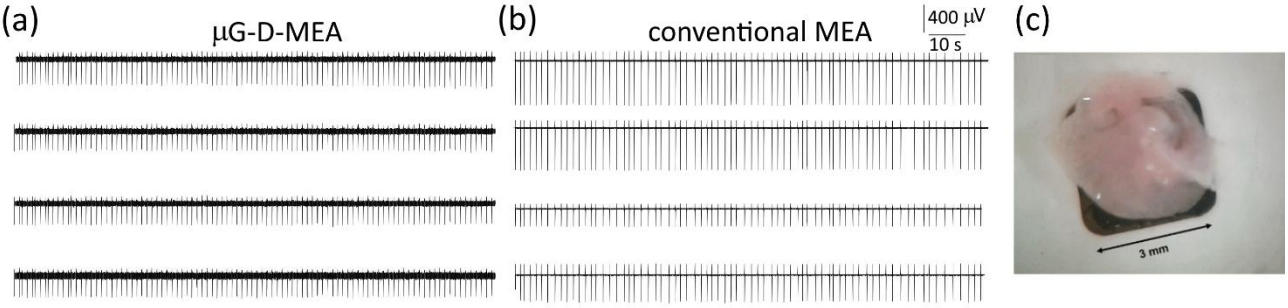

Figure 5 – Potentiometric recording of action potentials from a sinoatrial node performed with four representative electrodes of µG-D-MEA (a) and conventional MEA (b). (c) Optical image of the tissue placed over the sensor.

During the measurements with the µG-D-MEA, the modulation of electrical activity was also studied by delivering drugs to the tissue under investigation. A control trace was recorded maintaining the SA node into

a physiological 2 mM Ca^{2+} solution. Under this control condition, the signals exhibited a rhythmic generation with mean amplitude of (-210 ± 20) µV at the above-mentioned basal frequency. Subsequently, a solution containing 10 µM of the L-type calcium channel (LTCC) agonist BayK 8644 was added to increase the Ca^{2+} fluxes through LTCCs to increase the frequency and rate of rise of cardiac APs (figure 6a).

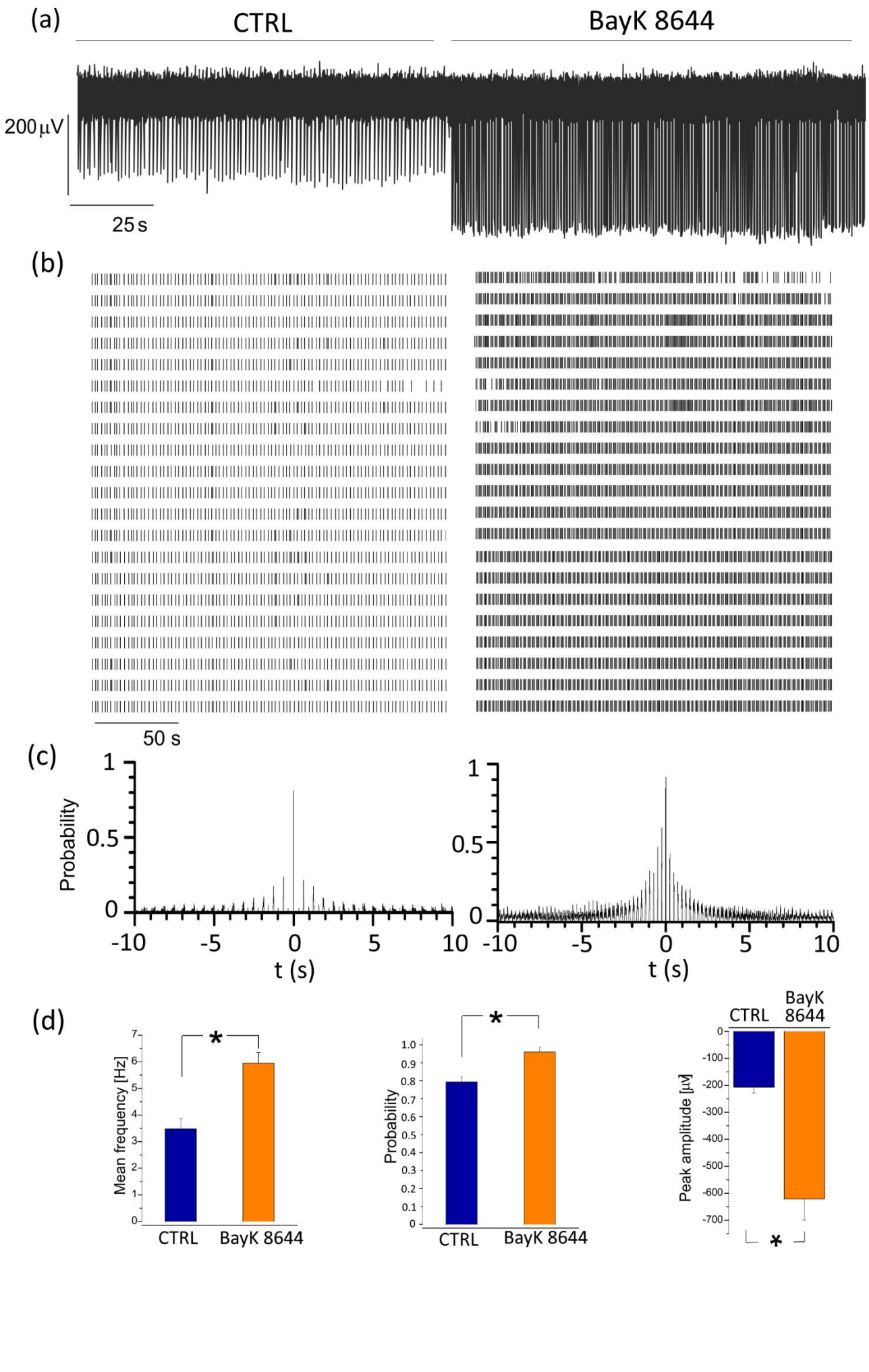
(a)
CTRL
BayK 8644
200 µV
25 s
(b)
50 s
(c)
Probability
1
0.5
0
-10
-5
0
5
10
t (s)
(d)
Mean frequency [Hz]
CTRL
BayK 8644
Probability
Peak amplitude [µM]
*

Figure 6 – (a) Representative potentiometric traces of sinoatrial node spontaneous activity (CTRL) before and during addition of BayK 8644 (10 μM.) (b) Raster plot showing the activity from different channels in control (left) and with BayK 8644 (right). (c) probability vs time diagrams indicating the cross-correlation between a reference electrode and others representative channels (d) The histograms represent the mean values of the firing frequency (left), the cross-correlation probability (middle) and the peak amplitude (right) of the detected signals, under control conditions and during application of BayK 8644.

In the presence of BayK 8644, a significant enhancement of spontaneous action potentials frequency (from (3.5 ± 0.4) Hz to (4.4 ± 0.4) Hz), AP amplitude ((-210 ± 20) μV to (-620 ± 80) μV) and AP synchronization can be observed (figure 6). The increased firing frequency observed in the presence of BayK 8644 was coherent with the role exerted by LTCCs on SA node [68] and other cells [69]. Similarly, the effect induced by BayK 8644 on extracellularly recorded AP amplitude is associated with the increased rate of AP rising phase. The effect of BayK 8644 on AP synchronization is caused as well by the longer open time of LTCCs induced by the above-mentioned agonist and can be evaluated by the cross-correlograms (figure 6c). Fig. 6c represents the cross-correlation probability vs time graph and quantifies the degree of synchronization between signals detected by different recordings electrodes. In particular, it reports a higher value of probability for short delay time indicating a good synchronization on the signals generation performed by all the cells of the sinoatrial node tissue. As expected, this effect is further improved by the administration of BayK 8644 (increasing of the cross-correlation probability from 0.79 ± 0.03 to 0.96 ± 0.03). Finally, a cadmium-enriched solution (500 μM) was delivered to inhibit cardiac AP generation (figure 2SM) ensuring the absence of artefacts in the recorded traces.

The previous measurements demonstrated the possibility of detecting APs by means of potentiometric measurements from excitable tissues. In the following, experiments carried on hippocampal neurons plated and cultured on the device surfaces, are reported. The investigation of neurons, with respect to the sinoatrial node, requires a proper cell adhesion on the surface device and the capability of detecting on average faster signals (i.e. FWHM of few ms) of lower amplitude (i.e. few tens of μV). Also for these measurements, four representative recordings obtained from independent electrodes of μG-D-MEA and conventional MEA are shown (figure 7).

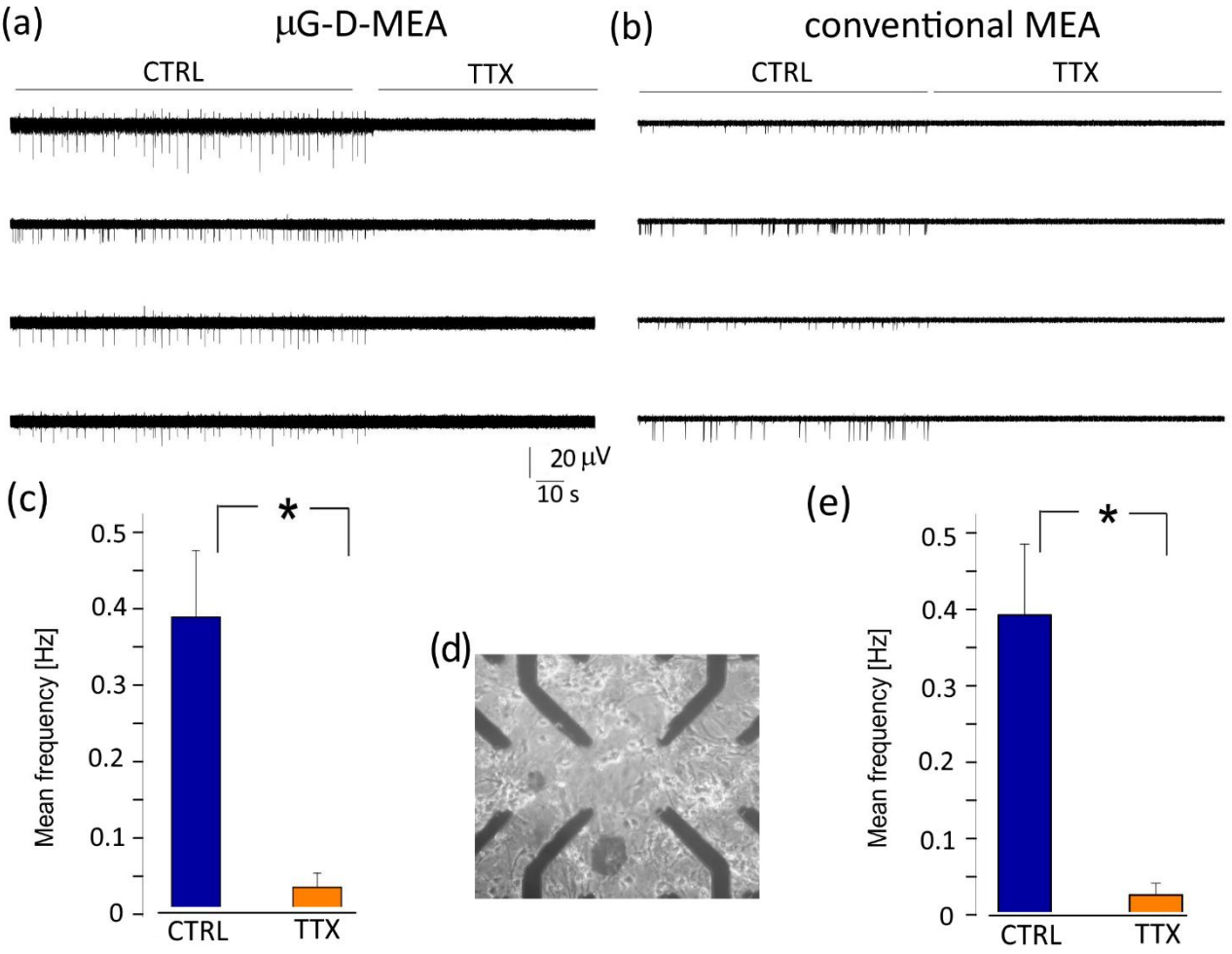

Figure 7 - Potentiometric recording of APs from 12 DIV hippocampal neurons, under control conditions and in the presence of TTX. Four representative electrodes of μG-D-MEA (a) and conventional MEA (b) are shown. Related histograms of signals frequency are reported in panel (c) for the μG-D-MEA and (e) for the conventional MEA. (d) Optical micrograph of cultured hippocampal neurons on the μG-D-MEA.

The traces show spontaneous APs occurring with (0.39 ± 0.04) Hz and (0.34 ± 0.02) Hz mean frequency, respectively for the μG-D-MEA and the conventional MEA (frequencies values compatible with an ANOVA test followed by Bonferroni *post hoc* comparison $p > 0.05$). In order to suppress the spontaneous electrical activity of the neuronal network, the Na^+ channel blocker tetrodotoxin (TTX, 300 nM) was added to the extracellular solution, thus confirming the absence of instrumental artefacts [70,71]. The recordings confirm the applicability of the μG-D-MEA for the detection of APs also from cultured neurons plated directly on the sensor surface.

3 Conclusions

In the present paper, we report on the fabrication, characterization and *in vitro* functional validation of diamond-based multi-electrode arrays developed for the detection of APs and exocytotic events from excitable cells. The technique employed for the fabrication of these devices is the ion beam lithography, which allows the creation of graphitic micro-patterns into the diamond matrix. This approach allows the fabrication of full carbon sensors combining both the properties of diamond (i.e. biocompatibility, chemical inertness) employed as a growth substrate and of graphite (i.e. electrical conduction) working as sensing electrodes for the cellular interfacing. The fabricated μG-D-MEA were characterized by means of Raman spectroscopy, mapping the diamond/graphite phase transition and concurrent mechanical stresses, and by electrical measurements evaluating the electrodes resistance and resistivity.

Finally, *in vitro* measurements from cultured neurons and cardiac tissue were performed in order to functionally validate the sensors for potentiometric and amperometric detection. Detection of quantal exocytotic events from dopaminergic midbrain neurons was shown by analysing the influence of the sampling frequency and electrodes bias on the amperometric spikes parameters. Potentiometric recordings from both the sinoatrial node and dissociated hippocampal neurons were reported, showing a perfect agreement comparing the data with those recorded with conventional MEA.

In conclusion, our work demonstrates that μG-D-MEAs are suitable devices for collecting signals adopting two different acquisition schemes: amperometry and potentiometry. This allows further step towards the creation of an all-carbon sensor capable of performing the simultaneous measurement of the neurotransmitter release (exocytosis) and AP firings from neuronal circuits, which would represent an innovative tool in neurosciences.

Acknowledgements

This work is supported by the following projects: DIACELL project (from National Institute of Nuclear Physics), MiRaDS project (from CRT foundation), “Finanziamento ex-post di progetti di ricerca di Ateneo” (from CSP foundation), “Departments of Excellence” (L. 232/2016) project (from Italian MIUR), project 2015FNWP34 (from Italian MIUR) and CSTO165284 (from Compagnia di San Paolo).

Ion beam irradiations were performed at the AN2000 accelerator of the Legnaro National Laboratories of the Italian Institute of Nuclear Physics (INFN) within the "Dia.Fab." beamtime.

We are grateful to Dr Claudio Franchino for cell culture preparation.

References

[1] W. Almers, Exocytosis, Annu. Rev. Physiol. 52 (1990) 607–624. doi:10.1146/annurev.ph.52.030190.003135.

[2] R. Jahn, T.C. Sudhof, Synaptic Vesicles and Exocytosis, Annu. Rev. Neurosci. 17 (1994) 219–246. doi:10.1146/annurev.ne.17.030194.001251.

[3] R.C. Lin, R.H. Scheller, Mechanisms of Synaptic Vesicle Exocytosis, Annu. Rev. Cell Dev. Biol. 16 (2000) 19–49. doi:10.1146/annurev.cellbio.16.1.19.

[4] B.P. Bean, The action potential in mammalian central neurons, Nat. Rev. Neurosci. 8 (2007) 451–465. doi:10.1038/nrn2148.

[5] G.W. Beeler, H. Reuter, Reconstruction of the action potential of ventricular myocardial fibres, J. Physiol. 268 (1977) 177–210. doi:10.1113/jphysiol.1977.sp011853.

[6] C. Juel, Muscle action potential propagation velocity changes during activity, Muscle Nerve. 11 (1988) 714–719. doi:10.1002/mus.880110707.

[7] F. Lemaître, M. Guille Collignon, C. Amatore, Recent advances in Electrochemical Detection of Exocytosis, Elsevier Ltd, 2014. doi:10.1016/j.electacta.2014.02.059.

[8] I. Suzuki, M. Fukuda, K. Shirakawa, H. Jiko, M. Gotoh, Carbon nanotube multi-electrode array chips for noninvasive real-time measurement of dopamine, action potentials, and

postsynaptic potentials, Biosens. Bioelectron. 49 (2013) 1–6. doi:10.1016/j.bios.2013.05.023.

[9] M. Alcaide, A. Taylor, M. Fjorback, V. Zachar, C.P. Pennisi, Boron-doped nanocrystalline diamond electrodes for neural interfaces: In vivo biocompatibility evaluation, Front. Neurosci. 10 (2016) 1–9. doi:10.3389/fnins.2016.00087.

[10] P.A. Nistor, P.W. May, F. Tamagnini, A.D. Randall, M.A. Caldwell, Long-term culture of pluripotent stem-cell-derived human neurons on diamond – A substrate for neurodegeneration research and therapy, Biomaterials. 61 (2015) 139–149. doi:10.1016/j.biomaterials.2015.04.050.

[11] L. Tang, C. Tsai, W.W.W.W. Gerberich, L. Kruckeberg, D.R.R. Kania, Biocompatibility of chemical-vapour-deposited diamond, Biomaterials. 16 (1995) 483–488. doi:10.1016/0142-9612(95)98822-V.

[12] L. Grieten, S.D. Janssens, A. Ethirajan, N. Vanden Bon, M. Ameloot, L. Michiels, K. Haenen, P. Wagner, Real-time study of protein adsorption on thin nanocrystalline diamond, Phys. Status Solidi Appl. Mater. Sci. 208 (2011) 2093–2098. doi:10.1002/pssa.201100122.

[13] F. Fontaine, E. Gheeraert, a. Deneuville, Conduction mechanisms in boron implanted diamond films, Diam. Relat. Mater. 5 (1996) 752–756. doi:10.1016/0925-9635(95)00383-5.

[14] T. Vogel, J. Meijer, A. Zaitsev, Highly effective p-type doping of diamond by MeV-ion implantation of boron, Diam. Relat. Mater. 13 (2004) 1822–1825. doi:10.1016/j.diamond.2004.04.005.

[15] T. Lühmann, R. Wunderlich, R. Schmidt-Grund, J. Barzola-Quiquia, P. Esquinazi, M. Grundmann, J. Meijer, Investigation of the graphitization process of ion-beam irradiated diamond using ellipsometry, Raman spectroscopy and electrical transport measurements, Carbon N. Y. 121 (2017) 512–517. doi:10.1016/j.carbon.2017.05.093.

[16] F. Picollo, P. Olivero, F. Bellotti, Ž. Pastuović, N. Skukan, A. Lo Giudice, G. Amato, M. Jakšić, E. Vittone, Formation of buried conductive micro-channels in single crystal diamond with MeV C and He implantation, Diam. Relat. Mater. 19 (2010) 466–469.

doi:10.1016/j.diamond.2010.01.005.

[17] V.P. Popov, L.N. Safronov, O. V. Naumova, D. V. Nikolaev, I.N. Kupriyanov, Y.N. Palyanov, Conductive layers in diamond formed by hydrogen ion implantation and annealing, in: Nucl. Instruments Methods Phys. Res. Sect. B Beam Interact. with Mater. Atoms, Elsevier B.V., 2012: pp. 100–107. doi:10.1016/j.nimb.2011.08.050.

[18] P. Olivero, G. Amato, F. Bellotti, O. Budnyk, E. Colombo, M. Jakšić, C. Manfredotti, Ž. Pastuović, F. Picollo, N. Skukan, M. Vannoni, E. Vittone, Direct fabrication of three-dimensional buried conductive channels in single crystal diamond with ion microbeam induced graphitization, Diam. Relat. Mater. 18 (2009) 870–876. doi:10.1016/j.diamond.2008.10.068.

[19] J. Park, J.J. Galligan, G.D. Fink, G.M. Swain, In vitro continuous amperometry with a diamond microelectrode coupled with video microscopy for simultaneously monitoring endogenous norepinephrine and its effect on the contractile response of a rat mesenteric artery, Anal. Chem. 78 (2006) 6756–6764. doi:10.1021/ac060440u.

[20] A. Pasquarelli, A. Marcantoni, D. Gavello, A. Battiato, F. Picollo, P. Olivero, E. Carbone, V. Carabelli, Simultaneous Fluorescent and Amperometric Detection Of Catecholamine Release From Neuroendocrine Cells With Transparent Diamond MEAs, Front. Neurosci. 10 (2016). doi:10.3389/conf.fnins.2016.93.00129.

[21] S. Gosso, M. Turturici, C. Franchino, E. Colombo, A. Pasquarelli, E. Carbone, V. Carabelli, Heterogeneous distribution of exocytotic microdomains in adrenal chromaffin cells resolved by high-density diamond ultra-microelectrode arrays, J. Physiol. 592 (2014) 3215–3230. doi:10.1113/jphysiol.2014.274951.

[22] V. Carabelli, S. Gosso, A. Marcantoni, Y. Xu, E. Colombo, Z. Gao, E. Vittone, E. Kohn, A. Pasquarelli, E. Carbone, Nanocrystalline diamond microelectrode arrays fabricated on sapphire technology for high-time resolution of quantal catecholamine secretion from chromaffin cells, Biosens. Bioelectron. 26 (2010) 92–98. doi:10.1016/j.bios.2010.05.017.

[23] V. Maybeck, R. Edgington, A. Bongrain, J.O. Welch, E. Scorsone, P. Bergonzo, R.B. Jackman, A. Offenhäusser, Boron-doped nanocrystalline diamond microelectrode arrays monitor cardiac action potentials, Adv. Healthc. Mater. 3 (2014) 283–289. doi:10.1002/adhm.201300062.

[24] M. McDonald, A. Monaco, F. Vahidpour, K. Haenen, M. Giugliano, M. Nesladek, Diamond microelectrode arrays for in vitro neuronal recordings, MRS Commun. 7 (2017) 683–690. doi:10.1557/mrc.2017.62.

[25] C. Hébert, E. Scorsone, A. Bendali, R. Kiran, M. Cottance, H.A. Girard, J. Degardin, E. Dubus, G. Lissorgues, L. Rousseau, P. Mailley, S. Picaud, P. Bergonzo, Boron doped diamond biotechnology: From sensors to neurointerfaces, Faraday Discuss. 172 (2014) 47–59. doi:10.1039/c4fd00040d.

[26] A.E. Hadjinicolaou, R.T. Leung, D.J. Garrett, K. Ganesan, K. Fox, D.A.X. Nayagam, M.N. Shivdasani, H. Meffin, M.R. Ibbotson, S. Prawer, B.J. O'Brien, Electrical stimulation of retinal ganglion cells with diamond and the development of an all diamond retinal prosthesis, Biomaterials. 33 (2012) 5812–5820. doi:10.1016/j.biomaterials.2012.04.063.

[27] A. Bendali, L. Rousseau, G. Lissorgues, E. Scorsone, M. Djilas, J. Dégardin, E. Dubus, S. Fouquet, R. Benosman, P. Bergonzo, J.A. Sahel, S. Picaud, Synthetic 3D diamond-based electrodes for flexible retinal neuroprostheses: Model, production and in vivo biocompatibility, Biomaterials. 67 (2015) 73–83. doi:10.1016/j.biomaterials.2015.07.018.

[28] G. Piret, C. Hébert, J.-P.P. Mazellier, L. Rousseau, E. Scorsone, M. Cottance, G. Lissorgues, M.O. Heuschkel, S. Picaud, P. Bergonzo, B. Yvert, 3D-nanostructured boron-doped diamond for microelectrode array neural interfacing, Biomaterials. 53 (2015) 173–183. doi:10.1016/j.biomaterials.2015.02.021.

[29] M. Bonnauron, S. Saada, L. Rousseau, G. Lissorgues, C. Mer, P. Bergonzo, High aspect ratio diamond microelectrode array for neuronal activity measurements, Diam. Relat. Mater. 17 (2008) 1399–1404. doi:10.1016/j.diamond.2007.12.065.

[30] P. Ariano, A. Lo Giudice, A. Marcantoni, E. Vittone, E. Carbone, D. Lovisolo, A diamond-based biosensor for the recording of neuronal activity., Biosens. Bioelectron. 24 (2009) 2046–2050. doi:10.1016/j.bios.2008.10.017.

[31] M. Dankerl, S. Eick, B. Hofmann, M.H.S. Ingebrandt, A. Offenhäusser, M. Stutzmann, J.A. Garrido, Diamond transistor array for extracellular recording from electrogenic cells, Adv. Funct. Mater. 19 (2009) 2915–2923. doi:10.1002/adfm.200900590.

[32] F. Picollo, A. Battiato, E. Bernardi, M. Plaitano, C. Franchino, S. Gosso, A. Pasquarelli, E. Carbone, P. Olivero, V. Carabelli, All-carbon multi-electrode array for real-time in vitro measurements of oxidizable neurotransmitters, Sci. Rep. 6 (2016) 20682. doi:10.1038/srep20682.

[33] F. Picollo, S. Gosso, E. Vittone, A. Pasquarelli, E. Carbone, P. Olivero, V. Carabelli, A new diamond biosensor with integrated graphitic microchannels for detecting quantal exocytic events from chromaffin cells, Adv. Mater. 25 (2013) 4696–4700. doi:10.1002/adma.201300710.

[34] F. Picollo, A. Battiato, E. Bernardi, A. Marcantoni, A. Pasquarelli, E. Carbone, P. Olivero, V. Carabelli, Microelectrode arrays of diamond-insulated graphitic channels for real-time detection of exocytotic events from cultured chromaffin cells and slices of adrenal glands., Anal. Chem. 88 (2016) 7493–7499. doi:10.1021/acs.analchem.5b04449.

[35] S. Lagomarsino, P. Olivero, S. Calusi, D.G. Monticone, L. Giuntini, M. Massi, S. Sciortino, A. Sytchkova, A. Sordini, M. Vannoni, Complex refractive index variation in proton-damaged diamond, Opt. Express. 20 (2012) 19382–19394. doi:10.1364/OE.20.019382.

[36] M.A. Draganski, E. Finkman, B.C. Gibson, B.A. Fairchild, K. Ganesan, N. Nabatova-Gabain, S. Tomljenovic-Hanic, A.D. Greentree, S. Prawer, Tailoring the optical constants of diamond by ion implantation, Opt. Mater. Express. 2 (2012) 644–649. doi:10.1364/OME.2.000644.

[37] P. Olivero, S. Calusi, L. Giuntini, S. Lagomarsino, a. Lo Giudice, M. Massi, S. Sciortino, M.

Vannoni, E. Vittone, A. Lo Giudice, M. Massi, S. Sciortino, Controlled variation of the refractive index in ion-damaged diamond, Diam. Relat. Mater. 19 (2010) 428–431. doi:10.1016/j.diamond.2009.12.011.

[38] M. Mohr, F. Picollo, A. Battiato, E. Bernardi, J. Forneris, A. Tengattini, E. Enrico, L. Boarino, F. Bosia, H.J. Fecht, P. Olivero, Characterization of the recovery of mechanical properties of ion-implanted diamond after thermal annealing, Diam. Relat. Mater. 63 (2016) 75–79. doi:10.1016/j.diamond.2015.11.008.

[39] F. Bosia, N. Argiolas, M. Bazzan, P. Olivero, F. Picollo, a. Sordini, M. Vannoni, E. Vittone, Modification of the structure of diamond with MeV ion implantation, Diam. Relat. Mater. 20 (2011) 774–778. doi:10.1016/j.diamond.2011.03.025.

[40] R.A. Khmelnitsky, V.A. Dravin, A.A. Tal, E. V. Zavedeev, A.A. Khomich, A. V. Khomich, A.A. Alekseev, S.A. Terentiev, Damage accumulation in diamond during ion implantation, J. Mater. Res. 30 (2015) 1583–1592. doi:10.1557/jmr.2015.21.

[41] F. Bosia, S. Calusi, L. Giuntini, S. Lagomarsino, A. Lo Giudice, M. Massi, P. Olivero, F. Picollo, S. Sciortino, A. Sordini, M. Vannoni, E. Vittone, Finite element analysis of ion-implanted diamond surface swelling, Nucl. Instruments Methods Phys. Res. Sect. B Beam Interact. with Mater. Atoms. 268 (2010) 2991–2995. doi:10.1016/j.nimb.2010.05.025.

[42] P. Olivero, J. Forneris, M. Jakšić, Z. Pastuović, F. Picollo, N. Skukan, E. Vittone, Focused ion beam fabrication and IBIC characterization of a diamond detector with buried electrodes, Nucl. Instruments Methods Phys. Res. Sect. B Beam Interact. with Mater. Atoms. 269 (2011) 2340–2344. doi:10.1016/j.nimb.2011.02.021.

[43] R. Kalish, S. Prawer, Graphitization of diamond by ion impact: Fundamentals and applications, Nucl. Instruments Methods Phys. Res. Sect. B Beam Interact. with Mater. Atoms. 106 (1995) 492–499. doi:10.1016/0168-583X(95)00758-X.

[44] A. Gippius, R.A.R. Khmelnitskiy, V.A. Dravin, S.D. Tkachenko, Formation and characterization of graphitized layers in ion-implanted diamond, Diam. Relat. Mater. 8

(1999) 1631–1634. doi:10.1016/S0925-9635(99)00047-3.

[45] A. Battiato, M. Lorusso, E. Bernardi, F. Picollo, F. Bosia, D. Ugues, A. Zelferino, A. Damin, J. Baima, N.M. Pugno, E.P. Ambrosio, P. Olivero, Softening the ultra-stiff: Controlled variation of Young's modulus in single-crystal diamond by ion implantation, Acta Mater. 116 (2016) 95–103. doi:10.1016/j.actamat.2016.06.019.

[46] J.F. Ziegler, M.D. Ziegler, J.P. Biersack, SRIM - The stopping and range of ions in matter (2010), Nucl. Instruments Methods Phys. Res. Sect. B Beam Interact. with Mater. Atoms. 268 (2010) 1818–1823. doi:10.1016/j.nimb.2010.02.091.

[47] A. Re, D. Angelici, A. Lo Giudice, J. Corsi, S. Allegretti, A.F. Biondi, G. Gariani, S. Calusi, N. Gelli, L. Giuntini, M. Massi, F. Taccetti, L. La Torre, V. Rigato, G. Pratesi, Ion Beam Analysis for the provenance attribution of lapis lazuli used in glyptic art: The case of the "Collezione Medicea," Nucl. Instruments Methods Phys. Res. Sect. B Beam Interact. with Mater. Atoms. 348 (2015) 278–284. doi:10.1016/j.nimb.2014.11.060.

[48] A. Lo Giudice, P. Olivero, C. Manfredotti, M. Marinelli, E. Milani, F. Picollo, G. Prestopino, A. Re, V. Rigato, C. Verona, G. Verona-Rinati, E. Vittone, Lateral IBIC characterization of single crystal synthetic diamond detectors, Phys. Status Solidi - Rapid Res. Lett. 5 (2011) 80–82. doi:10.1002/pssr.201004488.

[49] V. Rigato, Interdisciplinary physics with small accelerators at LNL: Status and perspectives, AIP Conf. Proc. 1530 (2013) 29–34. doi:10.1063/1.4812902.

[50] C. Hepp, T. Müller, V. Waselowski, J.N. Becker, B. Pingault, H. Sternschulte, D. Steinmüller-Nethl, A. Gali, J.R. Maze, M. Atatüre, C. Becher, Electronic Structure of the Silicon Vacancy Color Center in Diamond, Phys. Rev. Lett. 112 (2014) 036405. doi:10.1103/PhysRevLett.112.036405.

[51] G. Prestopino, M. Marinelli, E. Milani, C. Verona, Photo-physical properties of He-related color centers in diamond, Appl. Phys. Lett. 111 (2017) 1–9. doi:10.1063/1.4996825.

[52] J. Forneris, A. Tengattini, S.D. Tchernij, F. Picollo, A. Battiato, P. Traina, I.P. Degiovanni,

E. Moreva, G. Brida, V. Grilj, N. Skukan, M. Jakšić, M. Genovese, P. Olivero, Creation and characterization of He-related color centers in diamond, J. Lumin. 179 (2016) 59–63. doi:10.1016/j.jlumin.2016.06.039.

[53] A.C. Ferrari, Raman spectroscopy of graphene and graphite: Disorder, electron-phonon coupling, doping and nonadiabatic effects, Solid State Commun. 143 (2007) 47–57. doi:10.1016/j.ssc.2007.03.052.

[54] A.C. Ferrari, D.M. Basko, Raman spectroscopy as a versatile tool for studying the properties of graphene, Nat. Nanotechnol. 8 (2013) 235–246. doi:10.1038/nnano.2013.46.

[55] F. Picollo, D. Gatto Monticone, P. Olivero, B. a. Fairchild, S. Rubanov, S. Prawer, E. Vittone, Fabrication and electrical characterization of three-dimensional graphitic microchannels in single crystal diamond, New J. Phys. 14 (2012) 053011. doi:10.1088/1367-2630/14/5/053011.

[56] S. Prawer, R.J. Nemanich, Raman spectroscopy of diamond and doped diamond, Philos. Trans. R. Soc. A Math. Phys. Eng. Sci. 362 (2004) 2537–2565. doi:10.1098/rsta.2004.1451.

[57] B. Sotillo, A. Chiappini, V. Bharadwaj, J.P. Hadden, F. Bosia, P. Olivero, M. Ferrari, R. Ramponi, P.E. Barclay, S.M. Eaton, Polarized micro-Raman studies of femtosecond laser written stress-induced optical waveguides in diamond, Appl. Phys. Lett. 112 (2018) 112. doi:10.1063/1.5017108.

[58] P. Olivero, F. Bosia, B. a. Fairchild, B.C. Gibson, a. D. Greentree, P. Spizzirri, S. Prawer, Splitting of photoluminescent emission from nitrogen-vacancy centers in diamond induced by ion-damage-induced stress, New J. Phys. 15 (2013). doi:10.1088/1367-2630/15/4/043027.

[59] P. Olivero, G. Amato, F. Bellotti, S. Borini, a. Lo Giudice, F. Picollo, E. Vittone, Direct fabrication and IV characterization of sub-surface conductive channels in diamond with MeV ion implantation, Eur. Phys. J. B. 75 (2010) 127–132. doi:10.1140/epjb/e2009-00427-5.

[60] H.O. Pierson, Graphite Structure and Properties, in: Handb. Carbon, Graph. Diamonds Fullerenes, Elsevier, 1993: pp. 43–69. doi:10.1016/B978-0-8155-1339-1.50008-6.

[61] V. Carabelli, A. Marcantoni, F. Picollo, A. Battiato, E. Bernardi, A. Pasquarelli, P. Olivero, E. Carbone, Planar Diamond-Based Multiarrays to Monitor Neurotransmitter Release and Action Potential Firing: New Perspectives in Cellular Neuroscience, ACS Chem. Neurosci. 8 (2017) 252–264. doi:10.1021/acschemneuro.6b00328.

[62] J.D. Machado, a Morales, J.F. Gomez, R. Borges, cAmp modulates exocytotic kinetics and increases quantal size in chromaffin cells., Mol. Pharmacol. 60 (2001) 514–520. http://www.pubmedcentral.nih.gov/articlerender.fcgi?artid=1831689&tool=pmcentrez&rendertype=abstract.

[63] J.M. Finnegan, K. Pihel, P.S. Cahill, L. Huang, S.E. Zerby, a G. Ewing, R.T. Kennedy, R.M. Wightman, Vesicular quantal size measured by amperometry at chromaffin, mast, pheochromocytoma, and pancreatic beta-cells., J. Neurochem. 66 (1996) 1914–1923. doi:10.1046/j.1471-4159.1996.66051914.x.

[64] E.N. Pothos, V. Davila, D. Sulzer, Presynaptic recording of quanta from midbrain dopamine neurons and modulation of the quantal size., J. Neurosci. 18 (1998) 4106–4118.

[65] D. Sulzer, S.J. Cragg, M.E. Rice, Striatal dopamine neurotransmission: Regulation of release and uptake, Basal Ganglia. 6 (2016) 123–148. doi:10.1016/j.baga.2016.02.001.

[66] B.J. Venton, R.M. Wightman, Psychoanalytical Electrochemistry: Dopamine and Behavior, Anal. Chem. 75 (2003) 414 A-421 A. doi:10.1021/ac031421c.

[67] S.E. Hochstetler, M. Puopolo, S. Gustincich, E. Raviola, R.M. Wightman, Real-Time Amperometric Measurements of Zeptomole Quantities of Dopamine Released from Neurons, Anal. Chem. 72 (2000) 489–496. doi:10.1021/ac991119x.

[68] M.E. Mangoni, B. Couette, E. Bourinet, J. Platzer, D. Reimer, J. Striessnig, J. Nargeot, Functional role of L-type Cav1.3 Ca2+ channels in cardiac pacemaker activity, Proc. Natl. Acad. Sci. 100 (2003) 5543–5548. doi:10.1073/pnas.0935295100.

[69] A. Marcantoni, D.H.F. Vandael, S. Mahapatra, V. Carabelli, M.J. Sinnegger-Brauns, J. Striessnig, E. Carbone, Loss of Cav1.3 Channels Reveals the Critical Role of L-Type and BK

Channel Coupling in Pacemaking Mouse Adrenal Chromaffin Cells, J. Neurosci. 30 (2010) 491–504. doi:10.1523/JNEUROSCI.4961-09.2010.

[70] D. Gavello, J. Rojo-Ruiz, A. Marcantoni, C. Franchino, E. Carbone, V. Carabelli, Leptin Counteracts the Hypoxia-Induced Inhibition of Spontaneously Firing Hippocampal Neurons: A Microelectrode Array Study, PLoS One. 7 (2012) e41530. doi:10.1371/journal.pone.0041530.

[71] D. Gavello, C. Calorio, C. Franchino, F. Cesano, V. Carabelli, E. Carbone, A. Marcantoni, Early Alterations of Hippocampal Neuronal Firing Induced by Abeta42, Cereb. Cortex. 28 (2018) 433–446. doi:10.1093/cercor/bhw377.